


Article

Enhancing Sea Ice Inertial Oscillations in the Arctic Ocean between 1979 and 2019

Danqi Yuan ^{1,2}, Zhanjiu Hao ^{1,2}, Jia You ^{1,2}, Peiwen Zhang ^{1,3,4}, Baoshu Yin ^{1,2,3,4,5}, Qun Li ^{6,*} 
and Zhenhua Xu ^{1,3,4,5,*} 

¹ CAS Key Laboratory of Ocean Circulation and Waves, Institute of Oceanology, Chinese Academy of Sciences, Qingdao 266071, China

² University of Chinese Academy of Sciences, Beijing 100049, China

³ Pilot National Laboratory for Marine Science and Technology, Qingdao 266237, China

⁴ Center for Ocean Mega-Science, Chinese Academy of Sciences, Qingdao 266071, China

⁵ CAS Engineering Laboratory for Marine Ranching, Institute of Oceanology, Chinese Academy of Sciences, Qingdao 266071, China

⁶ MNR Key Laboratory for Polar Science, Polar Research Institute of China, Shanghai 200120, China

* Correspondence: liqun@pric.org.cn (Q.L.); xuzhenhua@qdio.ac.cn (Z.X.)

Abstract: As the Arctic Ocean continues to warm, both the extent and thickness of sea ice have dramatically decreased over the past few decades. These changes in ice have an impact on sea ice motion, including sea ice inertial oscillations (SIIO). However, the spatial pattern and temporal variations of Arctic SIIO remain poorly understood. In this study, the spatiotemporal characteristics of Arctic SIIO between 1979 and 2019 are revealed based on the sea ice drifting buoy dataset from the International Arctic Buoy Program (IABP). The results indicate the significant enhancement of SIIO during 1979–2019, with the trend of $7.84 \times 10^{-3} (\pm 3.34 \times 10^{-3}) \text{ a}^{-1}$ (a^{-1} means per year) in summer and $1.92 \times 10^{-3} (\pm 0.80 \times 10^{-3}) \text{ a}^{-1}$ in winter. Compared with the first 30 years, the magnitude of SIIO in 2009–2019 increases by 66% in summer and 21% in winter. Spatially, the remarkable enhancement of SIIO during 2009–2019 is found in most of the Arctic Ocean. Especially in summer, SIIO are significantly intensified in marginal seas, including the Beaufort Sea, East Siberian Sea and Laptev Sea, which is mainly correlated with the decrease of sea ice concentration in recent years. This study is anticipated to provide insights for spatiotemporal variation of Arctic sea ice inertial motion in recent decades.

Keywords: Arctic Ocean; sea ice drift; inertial oscillations; sea ice concentration; International Arctic Buoy Program



Citation: Yuan, D.; Hao, Z.; You, J.; Zhang, P.; Yin, B.; Li, Q.; Xu, Z. Enhancing Sea Ice Inertial Oscillations in the Arctic Ocean between 1979 and 2019. *Water* **2023**, *15*, 152. <https://doi.org/10.3390/w15010152>

Academic Editor: Changming Dong

Received: 20 November 2022

Revised: 26 December 2022

Accepted: 28 December 2022

Published: 30 December 2022



Copyright: © 2022 by the authors. Licensee MDPI, Basel, Switzerland. This article is an open access article distributed under the terms and conditions of the Creative Commons Attribution (CC BY) license (<https://creativecommons.org/licenses/by/4.0/>).

1. Introduction

Because of the continuous warmer Arctic Ocean, both the extent and thickness of sea ice have undergone a dramatic decline over the past few decades. The Arctic sea ice extent is shrinking at an average rate of 4.1% per decade, especially at a faster rate in summer [1–3]. Measurements from satellite sensors and submarines [4,5] also show a significant decrease in sea ice thickness. Meanwhile, multiyear ice has decreased by more than 50% from 2002 to 2017, reducing its coverage to less than one-third of the Arctic Ocean [5]. Now, Arctic sea ice is transitioning from a thick, strong ice pack to a thinner, less compact ice cover [6].

These changes in sea ice condition are accompanied by variation in ice kinematics, including sea ice drift, deformation and fracturing [7,8]. Sea ice motion is primarily driven by wind stress and ocean currents, and is also affected by the Coriolis force and the internal ice stress [9]. Sea ice motion plays a critical role in the ice thickness distribution [10–13] and the advection of ice mass out of the Arctic Ocean [14–16], and influences material and energy transfer between ocean and atmosphere [17,18]. The movement of sea ice can be tracked by satellite remote sensing technology and buoy observations. For a long time,

the Eulerian drift speed of sea ice has been derived from the sequential satellite remote sensing images, such as passive microwave and Synthetic Aperture Radar images [19–22]. The Lagrangian drift speed of sea ice can be derived from a GPS-equipped buoy fixed on the sea ice [23]. Using multiple-source datasets, the acceleration of sea ice drift in the Arctic Ocean in recent decades has been discovered [7,12,24,25]. Based on the drift trajectories of ice-tethered buoys, Lei et al. [26] suggested an accelerated southward drift of sea ice from the Central Arctic to the Fram Strait between 1979 and 2011.

Buoy observations with high-temporal-resolution sampling can provide information about high-frequency motions of sea ice, such as inertial oscillations, which cannot be well-resolved by satellite observations [27]. The observational results of buoys show inertial oscillations (with a period of about 12 h in the Arctic Ocean) to be substantial components of Arctic sea ice drift [28]. SIO are usually excited by sudden wind forcing changes and damped by the friction of ice-ocean interface and internal ice stresses due to the collision and fracturing of ice [29]. Based on two buoys deployed, respectively, in the summer of 2014 and 2016 in the western Arctic Ocean, Lei et al. [30] found strong inertial signals from the trajectories of both buoys and suggested that looser ice pack in 2016 attributed to enhanced sea ice inertial motion. Using buoy dataset from the International Arctic Buoy Program (IABP), Gimbert et al. [29] explored the spatiotemporal variation of SIO in the Arctic Ocean during 1979–2008 for the first time. The magnitude of SIO has significantly increased, which is considered a signature of the mechanical weakening of the Arctic ice cover. Considering that the Arctic sea ice is entering a new state of less coverage and more seasonal ice and the buoy observations become more intensive over the past ten years, it is necessary to study the characteristics and trends of the Arctic SIO in this new situation. This will further improve the forecast skill of sea-ice coupled models in simulating the subdaily timescale processes [31].

This study investigates the spatiotemporal characteristics of SIO in the Arctic Ocean over a longer period from the IABP buoy dataset, 1979–2019. Our results are anticipated to provide insights for the spatial and temporal variation of Arctic sea ice inertial motion over the past 41 years. This paper is organized as follows: Section 2 describes the IABP buoy dataset and its quality control as well as methods. In Section 3, the long-term trend of sea ice drift speed and the spatial distributions and temporal variation of SIO in the Arctic Ocean are analyzed. Section 4 discusses the impact of the buoy sampling inhomogeneity and the Arctic tides. Section 5 provides the conclusions.

2. Materials and Methods

2.1. Data

In order to better understand the spatial distributions and long-term variation of SIO in the context of a decrease in Arctic sea ice, the buoy dataset from IABP is used in this study. IABP aims to maintain a network of drifting buoys in the Arctic Ocean and provide meteorological and oceanic data for real-time operational requirement and research purposes. These buoys, equipped with several sensors (e.g., barometers measuring atmospheric pressure, thermistors measuring temperature) are fixed on the ice and move together with the ice cover. Horizontal position information can be obtained by GPS or Argo on drifting buoys and is used to calculate the speed of sea ice. The position data, with a 3 h-resolution from January 1979 to December 2016 and approximately a 1 h-resolution from January 2017 to December 2019, are adequate for the analysis of inertial motion (publicly available on the Web at <https://iabp.apl.uw.edu/data.html> (accessed on 27 December 2022)).

Although IABP data has been standardized, further quality control is still needed to facilitate the reliability of high-frequency motion analysis. Quality control of the dataset from 1979 to 2016 with a 3 h-resolution is as follows:

1. The “abrupt points” in a continuous buoy trajectory, that is, the points exceeding 1° distance of adjacent points, are removed as missing points, and the location information is replaced by linearly interpolating between adjacent positions. When the latitude is poleward of 82° N, we consider only the longitude difference between two positions;

2. We filter the trajectories containing errors caused by excessive satellite localization frequency and delete the corresponding position points;
3. We eliminate unrealistic speed values larger than 130 km d^{-1} .

Quality control for the data with a resolution of 1 h during 2017–2019 is also based on the above steps, except for the adjustment of distance threshold in step 1 from 1° to $1/3^\circ$. After quality control, the dataset in 2017–2019 is interpolated linearly to a 3 h-resolution.

We obtain 2194 buoy data files (note that the buoy tracks with a time span longer than one year are divided into multiple files by year) for the study of sea ice motion, consisting of 2.7×10^6 points at a resolution of 3 h for 1979–2019. Each buoy position is projected on a polar stereographic coordinate system centered on the North Pole, noted as $x\vec{e}_1 + y\vec{e}_2$, where \vec{e}_1 and \vec{e}_2 are two orthogonal unit vectors with \vec{e}_2 along the Greenwich Meridian. The study domain is delimited by the black thick dashed line in Figure 1b. The buoy positions further than 150 km away from the coasts are selected to avoid some aliases possibly caused by tides and coastal waves. The heterogeneity of the buoy data files and buoy tracks distribution significantly reflects the implementation of large international programs during different periods (Figure 1). As shown in Figure 1a, the number of buoy data files increased significantly during 2007–2008, and this was closely related to the International Polar Year (IPY, 2007–2008), when a large number of buoys were laid in the eastern and western Arctic Ocean. After that, the automatic observation technology and buoy number deployed in the Arctic has been qualitatively improved because a series of international programs have been implemented over the past decade, such as the Marginal Ice Zone observational program implemented in recent years (MIZ, 2012–2017), the Stratified Ocean Dynamics in the Arctic (SODA, 2016–2021) and the Multidisciplinary drifting Observatory for the Study of Arctic Climate (MOSAiC, 2019–2020).

In addition to the IABP dataset, the passive-microwave-derived sea ice concentration (SIC) provided by the National Snow and Ice Data Center (NSIDC, publicly available on the Web at <https://nsidc.org/data/g02202/versions/4> (accessed on 27 December 2022)) is used to investigate the spatiotemporal variation of SIC in the Arctic Ocean over recent years. This dataset has a spatial resolution of $25 \text{ km} \times 25 \text{ km}$ and a temporal resolution of 1d.

2.2. Methods

The frequency of inertial oscillations is characterized by $f_0 = 2\sin\varphi$ cycles d^{-1} , where φ is the latitude. From 70° N to 90° N , f_0 varies from 1.88 to 2 cycles d^{-1} . In the Arctic Ocean, inertial oscillations are not easily isolated from the semi-diurnal tide in the temporal filter due to their similar frequencies [32–34]. Thus, the rotary spectrum of the buoy velocity can be used to distinguish the signals of inertial oscillations and tidal forcing by complex Fourier transform, because the inertial oscillations feature a clockwise rotation in the Arctic Ocean. Before calculating the rotary spectrum, the two velocity components, that is, u_x and u_y , are computed from the buoy position data by

$$u_x(\tilde{x}, \tilde{y}, \tilde{t}) = \frac{x(t + \Delta t) - x(t)}{\Delta t}, \quad (1)$$

$$u_y(\tilde{x}, \tilde{y}, \tilde{t}) = \frac{y(t + \Delta t) - y(t)}{\Delta t}, \quad (2)$$

with $\Delta t = 3 \text{ h}$ and the mid-point $(\tilde{x}, \tilde{y}, \tilde{t})$ defined as: $\tilde{x} = [x(t + \Delta t) + x(t)]/2$, $\tilde{y} = [y(t + \Delta t) + y(t)]/2$, $\tilde{t} = [(t + \Delta t) + t]/2$. The complex Fourier transformation $\hat{U}(w)$ of u_x and u_y is defined as

$$\hat{U}(w) = \frac{1}{N} \sum_{t=t_0}^{t=t_{\text{end}}-\Delta t} e^{-i\omega t} (u_x + iu_y), \quad (3)$$

where N is the number of velocity samples; t_0 and t_{end} are the starting and final time of the temporal window for a selected buoy trajectory; $\omega = 2\pi f$ is the angular frequency; $f = 2\sin\varphi$ is the Coriolis frequency and $f > 0$ and $f < 0$ represent the counterclockwise

and clockwise rotation of buoy drift, respectively. Because tidal oscillation can be considered nearly as irrotational motion in the Arctic Ocean, the spectral peaks associated with semi-diurnal tides can be observed at both positive and negative frequencies. Based on the first-order approximation, the peaks associated with semi-diurnal tides are assumed to be roughly symmetrical between positive and negative frequency bands [29]. Owing to the superposition of inertial and semi-diurnal frequencies in the Arctic Ocean, the spectral peaks observed at $f \approx -2 \text{ cycles d}^{-1}$ are associated with inertial oscillations and semi-diurnal tides. The peaks observed at $f \approx 2 \text{ cycles d}^{-1}$ approximately represent the magnitude of semi-diurnal tides.

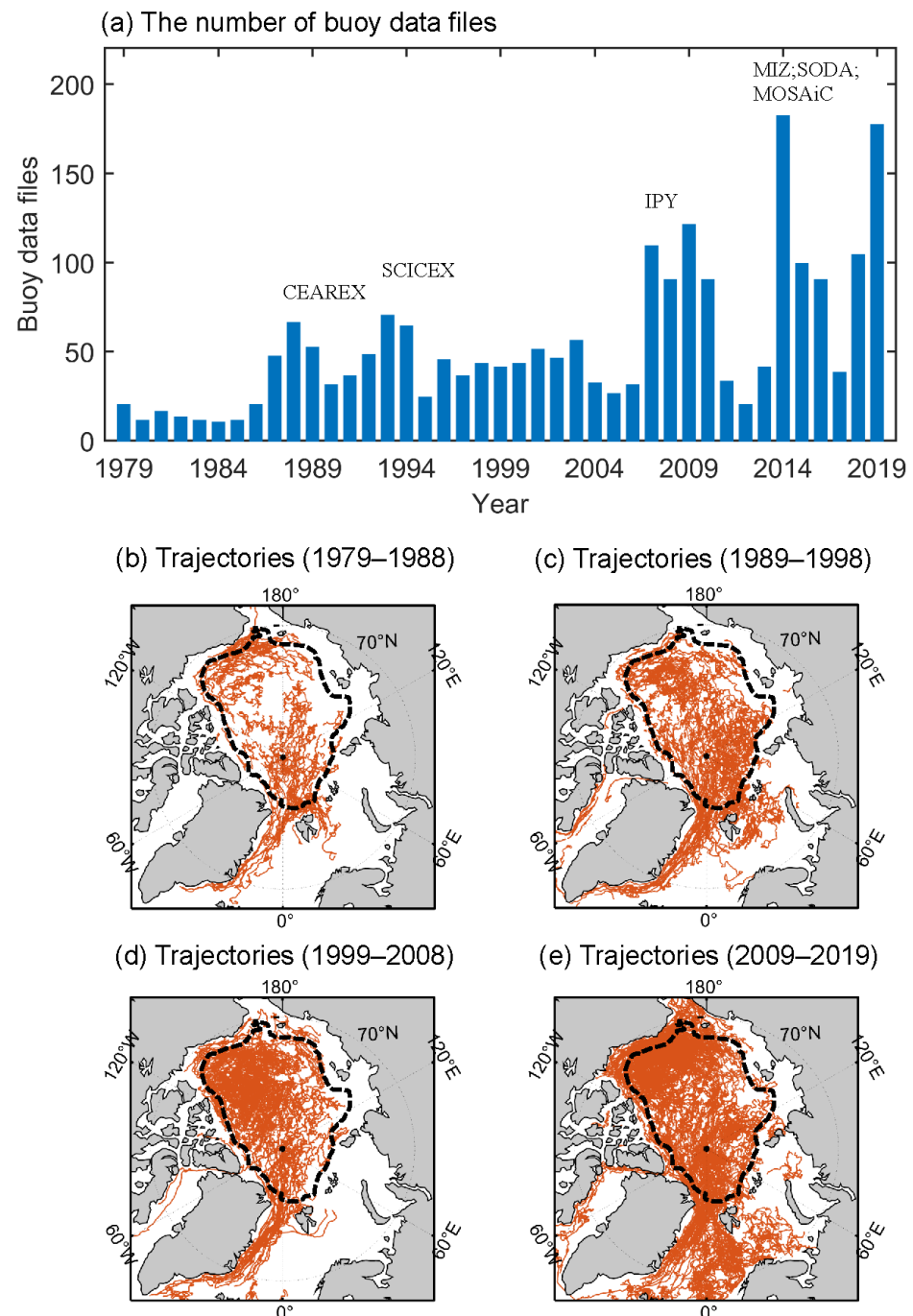


Figure 1. (a) The number of buoy data files available in this study from IABP between 1979 and 2019. Relevant large international programs are marked at the corresponding time points, including the Coordinated Eastern Arctic Experiment (CEAREX, 1988–1989); Submarine Arctic Science Program (SCICEX, 1993–); International Polar Year (IPY, 2007–2008); Marginal Ice Zone observational program

(MIZ, 2012–2017); Stratified Ocean Dynamics in the Arctic (SODA, 2016–2021); and Multidisciplinary drifting Observatory for the Study of Arctic Climate (MOSAiC, 2019–2020). Maps of sea ice drifting buoy trajectories in four decades: (b) 1979–1988; (c) 1989–1998; (d) 1999–2008; and (e) 2009–2019. The study domain is delimited by black thick dashed line.

Mooring observations in the Pacific sector of the Arctic Ocean showed that inertial oscillations of sea ice drift became strong during the formation and decay periods of ice, which corresponds to warmer months [35]. The trajectory of buoy (ID: 300234067936870) passing nearby the mooring location is selected (black curve in Figure 2a). The trajectory nearby the mooring location (from 28 July to 26 August 2019) marked in the red box of Figure 2a is zoomed in, as shown in Figure 2b. Strong inertial oscillations are clearly characterized by the clockwise cycloidal loops (Figure 2b), also evidenced by a strong peak (27.5 km d^{-1}) at the frequency $f \approx -1.9 \text{ cycles d}^{-1}$ in the rotary spectrum (Figure 2c). In addition, from the rotation spectrum, there is no significant tidal peak around this region with a value of zero at $f \approx 2 \text{ cycles d}^{-1}$, which is consistent with the in situ observation [35].

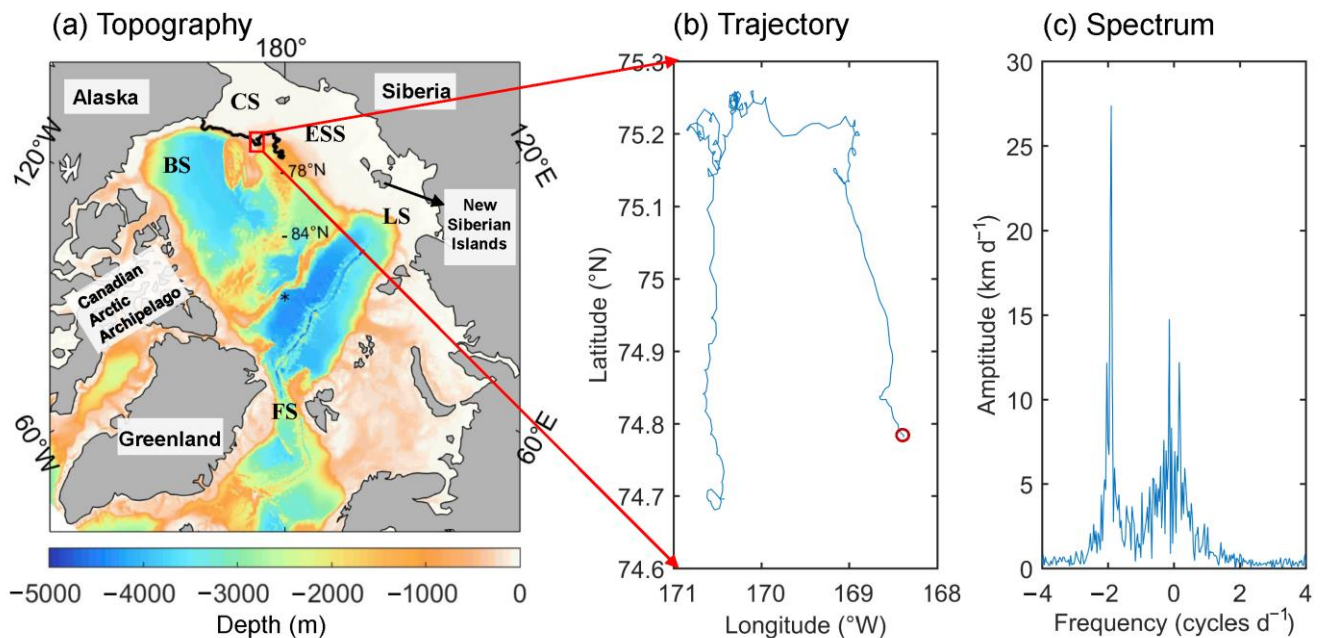


Figure 2. (a) Topography of the Arctic Ocean. Black curve represents the trajectory of buoy (ID: 300234067936870) in 2019. BS: Beaufort Sea; CS: Chukchi Sea; ESS: East Siberian Sea; LS: Laptev Sea; FS: Fram Strait. (b) The trajectory marked by the red box in (a) from 28 July to 26 August is magnified. The start point is marked by the red circle. (c) Rotary spectrum of the buoy drift velocity.

To quantify the intensity of sea ice inertial motion, this paper follows the definition of the non-dimensional parameter M given by Gimbert et al. [29]. For a given buoy position $(x_{pst}, y_{pst}, t_{pst})$, a new velocity time series at time t_{pst} , $W_{pst}(t)$, is obtained by a sliding window function, $g_{pst}(t)$:

$$W_{pst}(t) = U_b(t)g_{pst}(t), \quad (4)$$

$$g_{pst}(t) = \exp\left(\frac{-(t - t_{pst})^2}{2(nT_0)^2}\right), \quad (5)$$

where $U_b(t) = u_x(t)\vec{e}_1 + u_y(t)\vec{e}_2$. $g_{pst}(t)$ is a Gaussian window function defined by Gimbert et al. [29], in which T_0 is the inertial period ($1/f_0$) and n is set to 1. The temporal window of 3 days used in this study is long enough to explore variation of subdaily signals and short

enough to suppress multiday or longer signals. The rotary spectrum at inertial frequency $\hat{W}_{pst}(f_0)$ can be obtained by the complex Fourier transform:

$$\hat{W}_{pst}(f_0) = \Delta t \sum_{t=t_0}^{t_{end}} W_{pst}(t) e^{-i\omega_0 t}, \quad (6)$$

Finally, the value of $\hat{W}_{pst}(f_0)$ at time t_{pst} is normalized to obtain a non-dimensional parameter M :

$$M = \frac{|\hat{W}_{pst}(f_0)|}{\int_{t_0}^{t_{end}} g_{pst}(t) dt} \times \frac{4}{\pi \bar{W}_{pst}}, \quad (7)$$

where $\bar{W}_{pst} = \frac{1}{\int_{t_0}^{t_{end}} g_{pst}(t) dt} \sum_{t=t_0}^{t_{end}} dt |W_{pst}(t)|$ is the mean speed for the series $W_{pst}(t)$ at time t_{pst} .

Due to the heterogeneity of the buoy data sampling, the estimations on the temporal variation of sea ice motion parameter inevitably come with errors and uncertainty. Therefore, it is necessary to conduct a certain error analysis and evaluation to ensure the rationality of the analysis results. The errors are all estimated by a bootstrap method [36], a resampling technique for estimating statistics about a population by sampling a dataset with replacement. Bootstrap estimators of standard errors can be computed by Monte Carlo algorithm, described as follows:

1. Following the bootstrap method [36], we draw a sample randomly from the original dataset $y = (x_1, x_2, \dots, x_n)$. Repeat the same operation and construct a large number (usually in hundreds) of bootstrap samples: $y^*(1), y^*(2), \dots, y^*(B)$;
2. Estimate the statistics of mean value for each bootstrap sample:

$$\hat{\theta}^*(b) = \frac{\sum_{b=1}^B y^*(b)}{B}, \quad b = 1, 2, \dots, B, \quad (8)$$

3. Calculate the standard deviation of $\hat{\theta}(y^*(b))$ defined as:

$$\hat{\sigma}_B = \left[\frac{\sum_{b=1}^B (\hat{\theta}^*(b) - \bar{\theta}^*)^2}{B-1} \right]^{\frac{1}{2}}. \quad (9)$$

3. Results

3.1. The Enhancement of Sea Ice Drift Speed

The long-term variation of sea ice drift speed in the Arctic Ocean between 1979 and 2019 is investigated based on the IABP buoy dataset. It should be noted that the “long-term” in this study refers to the period 1979–2019. The definition of season follows Gimbert et al. [29]: July to September is defined as the summer season, and the rest represent the winter. The sea ice drift speed is defined by $U = \sqrt{u_x^2 + u_y^2}$ in the study domain (dashed line in Figure 1b). The summer and winter datasets of sea ice drift speed are constructed first by sorting the U values during 1979–2019 into the corresponding dataset according to their seasons. Second, both the summer and winter datasets are divided equally into 15 successive bins to eliminate the effect of the uneven temporal sampling of buoys. Each bin contains approximately 3.8×10^4 values for the summer dataset and 10.0×10^4 values for the winter dataset, respectively. The average speed of each bin $\bar{u}_{bin} = (1/N) \sum_{t \in bin} U(t)$ in an average time $\bar{t}_{bin} = (1/N) \sum_{t \in bin} t$ is calculated independently. The errors are evaluated by the bootstrap method described in Section 2.2.

Figure 3 shows the temporal variations of sea ice drift speed in the Arctic Ocean for summer and winter between 1979 and 2019. The trends of ice drift speed are estimated using the error-weighted linear least square method (solid lines in Figure 3). Arctic sea ice drift speed shows significantly increasing trends in both seasons, with $0.18 (\pm 0.07) \text{ km d}^{-1} \text{ a}^{-1}$

(i.e., increasing by 32.7% per decade) in summer and $0.10 (\pm 0.04) \text{ km d}^{-1} \text{ a}^{-1}$ (i.e., increasing by 20.4% per decade) in winter. The results are compared with the previous estimations in the changing rates of Arctic sea ice drift speed based on different datasets (Table 1). Based on the IABP buoy dataset during 1979–2011, Olason and Notz [24] discovered that Arctic sea ice drift speed increased by $0.11 (\pm 0.03) \text{ km d}^{-1} \text{ a}^{-1}$ in August–October and $0.04 (\pm 0.03) \text{ km d}^{-1} \text{ a}^{-1}$ in December–March, which were lower speeds than those in this study. The inconsistency may partly result from the difference of seasonal definition. However, the time span of the datasets contributes a lot because the dataset used in this study covers data in the most recent 10 years, a period with a dramatic reduction in sea ice. During this period (2009–2019), a linear fit gives a trend of sea ice drift speed in the Arctic Ocean with $0.27 (\pm 0.53) \text{ km d}^{-1} \text{ a}^{-1}$ in summer and $0.13 (\pm 0.27) \text{ km d}^{-1} \text{ a}^{-1}$ in winter. It should be noted that the error bounds are twice as big as the mean trends, which may partly result from the few data sampling points (only six bins) in this period. However, the mean magnitude of speed during 2009–2019 increases 40% for summer and 31% for winter compared with 1979–2008. In addition, the trend of sea ice drift speed increases from $0.09 (\pm 0.7) \text{ km d}^{-1}$ to $0.18 (\pm 0.07) \text{ km d}^{-1}$ in summer (from $0.04 (\pm 0.04) \text{ km d}^{-1}$ to $0.10 (\pm 0.04) \text{ km d}^{-1}$ in winter) when the time span is extended from 1979–2008 to 1979–2019. Analyses of sea ice motion during 1979–2019 using the NSIDC dataset showed that sea ice drift speed in Arctic increases at a rate of $0.13 \text{ km d}^{-1} \text{ a}^{-1}$ in July–September and $0.08 \text{ km d}^{-1} \text{ a}^{-1}$ (a mean value) in the rest of the months [25]. This is comparable with the results in this study. The discrepancy may be caused by the different data source: the NSIDC dataset, a spatiotemporally uniform grid data, is retrieved from satellite imagery and merged with the wind reanalysis data and buoy position data [13]. Although the trends in sea ice drift speed acquired from different datasets are slightly different, all estimations reflect that the increasing rate in ice drift speed is independent of season. It also confirmed that the results based on the IABP dataset in this study are credible.

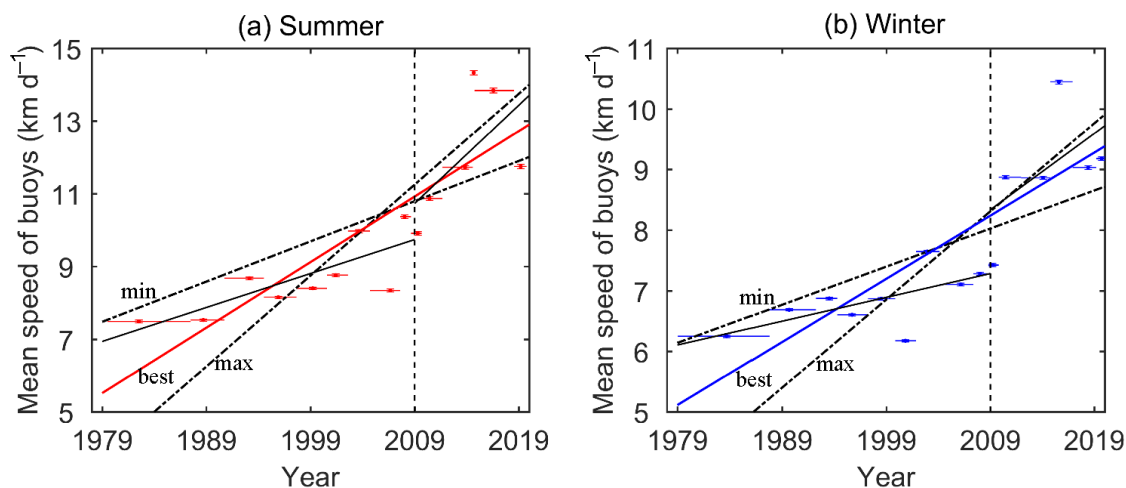


Figure 3. Multi-annual variation of sea ice drift speed $U(t)$ in (a) summer and (b) winter from January 1979 to December 2019. For each season, the data is equally divided into 15 successive bins. The mean value and error of each bin are independently estimated. The horizontal line represents the time span of each bin. The increasing rates (in the least square sense weighted by the errors) for 1979–2019, 1979–2008 and 2009–2019 are shown in each panel. The black dotted lines are error bounds of the rates for 1979–2019.

Table 1. Trends of sea ice drift speed in the Arctic Ocean obtained from this study and previous works.

	Data Source	Time Period	Seasonal Division and Changing Rates ($\text{km d}^{-1} \text{a}^{-1}$)
Zhang et al. [25]	Sea Ice Motion Vectors Version 4 dataset from NSIDC	1979–2019	0.08 (1 January–31 Mary) 0.04 (1 April–30 June) 0.13 (1 July–30 September) 0.11 (1 October–31 December)
Rampal et al. [7]	IABP buoy dataset	1979–2007	0.05 (15 June–30 September) 0.06 (1 December–15 May)
Olason and Notz [24]	IABP buoy dataset	1979–2011	0.11 (1 August–31 October) 0.04 (1 December–31 Mary)
Spreen et al. [37]	SSM/I satellite dataset	1992–2009	0.081 (1 October–31 May)
This study	IABP buoy dataset	1979–2019	0.18 (1 July–30 September) 0.10 (1 January–30 June, 1 October–31 December)

3.2. The SIIO Enhancement

In this section, the summer and winter datasets of the non-dimensional parameter M are constructed and then used to investigate the multi-annual variation of SIIO in the Arctic Ocean over the past four decades. The same as the method mentioned in Section 3.1, each dataset is equally split into 15 successive bins. As shown in Figure 4, the trend of average M value is $7.84 \times 10^{-3} (\pm 3.34 \times 10^{-3}) \text{ a}^{-1}$ (i.e., increasing by 69.13% per decade) in summer and $1.92 \times 10^{-3} (\pm 0.80 \times 10^{-3}) \text{ a}^{-1}$ (i.e., increasing by 13.85% per decade) in winter during 1979–2019, indicating a significant enhancement of SIIO. In addition, a linear fit gives a trend of the SIIO with $9.20 \times 10^{-3} (\pm 23.51 \times 10^{-3}) \text{ a}^{-1}$ in summer and $2.27 \times 10^{-3} (\pm 3.80 \times 10^{-3}) \text{ a}^{-1}$ in winter for 2009–2019. Similar to Section 3.1, there are also large error bounds of the increasing trends of SIIO during 2009–2019 owing to fewer data sampling points (only six bins). Compared with 1979–2008, the mean value of M significantly increases by 66% in summer and 21% in winter.

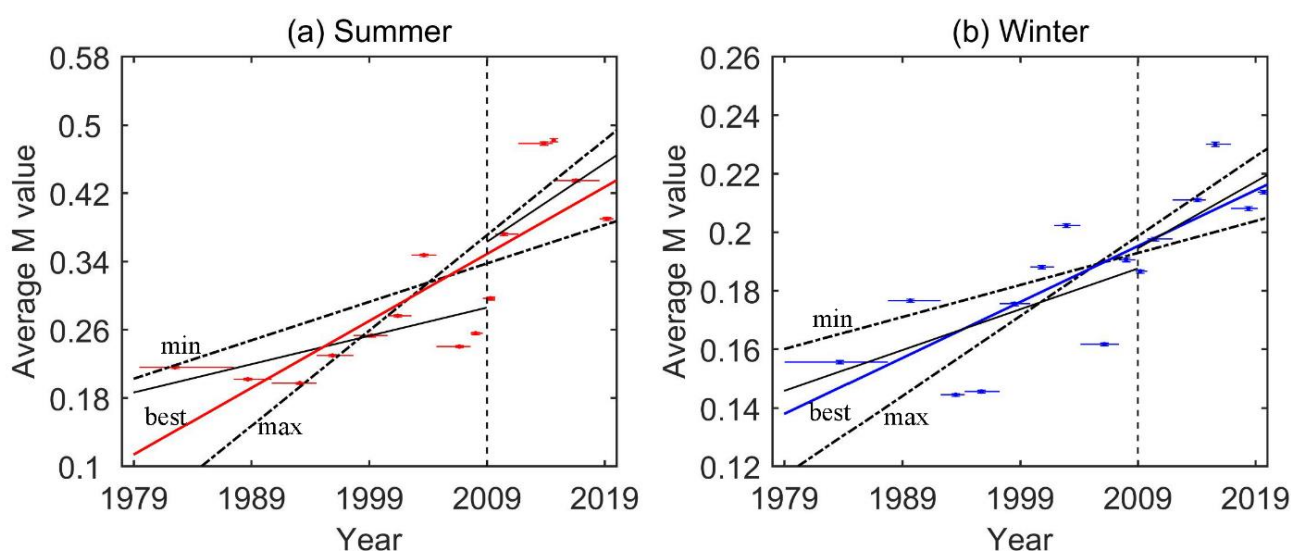


Figure 4. Multi-annual variation of sea ice inertial oscillation magnitude $M(t)$ in (a) summer and (b) winter from January 1979 to December 2019. For each season, the data is equally divided into 15 successive bins. The mean value and error of each bin are independently estimated. The horizontal line represents the time span of each bin. The increasing rates (in the least square sense weighted by the errors) for 1979–2019, 1979–2008, and 2009–2019 are shown in each panel. The black dotted lines are error bounds of the rates for 1979–2019.

Figure 5 displays the seasonal variations of M value in the Arctic Ocean. It is noteworthy that both the magnitude and increasing rate of SIIO in summer are more remarkable than those in winter (Figures 5 and 6). For 1979–2019, the M value reaches a minimum of 0.163 in December and a maximum of 0.342 in August, indicating a strong seasonal variability of SIIO, which agrees with the seasonal cycles of sea ice extent and thickness. Compared with 1979–2019 (blue curve), the seasonal variability in 2009–2019 is more remarkable (red curve), with larger M values in most months and a wider range. This further confirms the significant strengthening of SIIO during 2009–2019, especially in summer. Compared to 1979–2008 (black curve), the peak of M values in summer during 2009–2019 becomes steeper, with a maximum increase of 84.6% in July. This suggests that the thinner and less concentrated ice cover in summer in recent years is susceptible to external forcing and becomes more kinetic, thus leading to stronger inertial oscillations and the corresponding larger M values.

There are two main hypotheses for the increasing trend of SIIO over the past 41 years: strengthening external forcing and the thinning ice cover. Wind forcing is an important external factor driving sea ice motion. More than 70% of the variances of sea ice motion on the days-to-weeks timescales can be explained by local geostrophic wind [38,39]. Based on the wind data from four atmospheric reanalysis products (including the JRA, ERA-Interim, NCEP and NCEP-2), Spreen et al. [37] discovered that the wind speed in the Arctic Ocean slightly increased during 1992–2009 with a trend of 1–2% per decade. Zhang et al. [25] also drew a similar trend (increasing by 0.9% per decade) of Arctic wind speed during 1979–2019 based on the ERA-5 dataset. Regionally, the increase in wind speed was identified over most of the Arctic Ocean, with the most significant increase in the central Arctic Ocean, where the increasing trend of wind speed can partly account for the increased sea ice drift [37]. However, the changes of SIIO in the central Arctic Ocean are not significant (more details will be displayed in next section). While in other regions, the thinning ice cover is more likely to be the reason for the kinetic ice drift. Observation results from submarine sonars (1958–1976) and satellite sensors (2011–2018) showed that the average thickness of Arctic sea ice has decreased by 2.0 m (or 66%) over the past six decades. During 1999–2017, the multiyear ice also decreased more than 50% [5]. The thinning ice cover implies the decrease in mechanical strength and the increase in ice deformation and fracturing [40]. Consequently, the multi-annual variation of SIIO is mainly associated with the decrease in sea ice thickness.

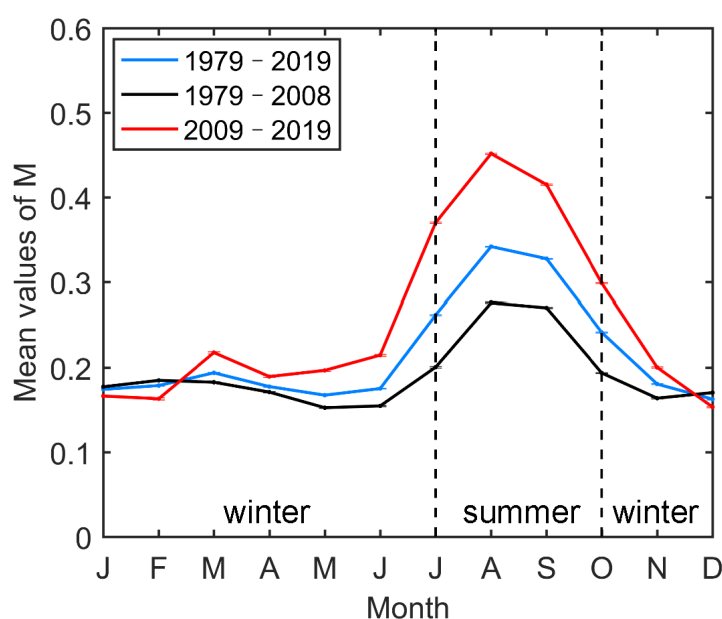


Figure 5. Seasonal variations of M values in 1979–2019 (blue line), 1979–2008 (black line) and 2009–2019 (red line). July, August and September constitute the summer, and the rest are winter.

3.3. Spatial Variation of SIIO

The spatial variation of SIIO is explored in this section. An uniform 25 km-resolution grid covering the Arctic Ocean is constructed. For each grid point (X_j, Y_j) , the spatially averaged M value, denoted as $\bar{M}(X_j, Y_j)$, is calculated by Equation (10) using the seasonal datasets of M as mentioned in Section 3.2.

$$\bar{M}(X_j, Y_j) = \frac{1}{\sum_i w_{ij}(x_i, y_i)} \sum_i w_{ij}(x_i, y_i) M_i(x_i, y_i), \quad (10)$$

The summation is performed for all points located in a circular region centered (X_j, Y_j) and with a radius of $L = 400$ km. The weight is defined as $w_{ij}(x_i, y_i) = e^{-d^2/2L^2}$, where $d = \sqrt{(x_i - X_j)^2 + (y_i - Y_j)^2}$ is the distance between the center point (X_j, Y_j) and other point (x_i, y_i) .

The spatial patterns of \bar{M} between 1979 and 2019 are shown in Figure 6a,d. It is found that SIIO are strong in marginal regions with low ice concentration and thin ice cover, including the Beaufort Sea and eastern Arctic Ocean. While in the north of the coasts of the Canadian Arctic Archipelago and Greenland, which are covered by multiyear ice throughout the year [41], inertial oscillations are relatively weak and even absent. The patterns for 1979–2008 and 2009–2019 are shown in Figure 6b,c,e,f. Compared with 1979–2008, the SIIO in most of the Arctic Ocean for 2009–2019 have strengthened, particularly in marginal seas during summer. The low-value zone of \bar{M} in the north of Canadian Arctic Archipelago and Greenland is also apparently shrinking.

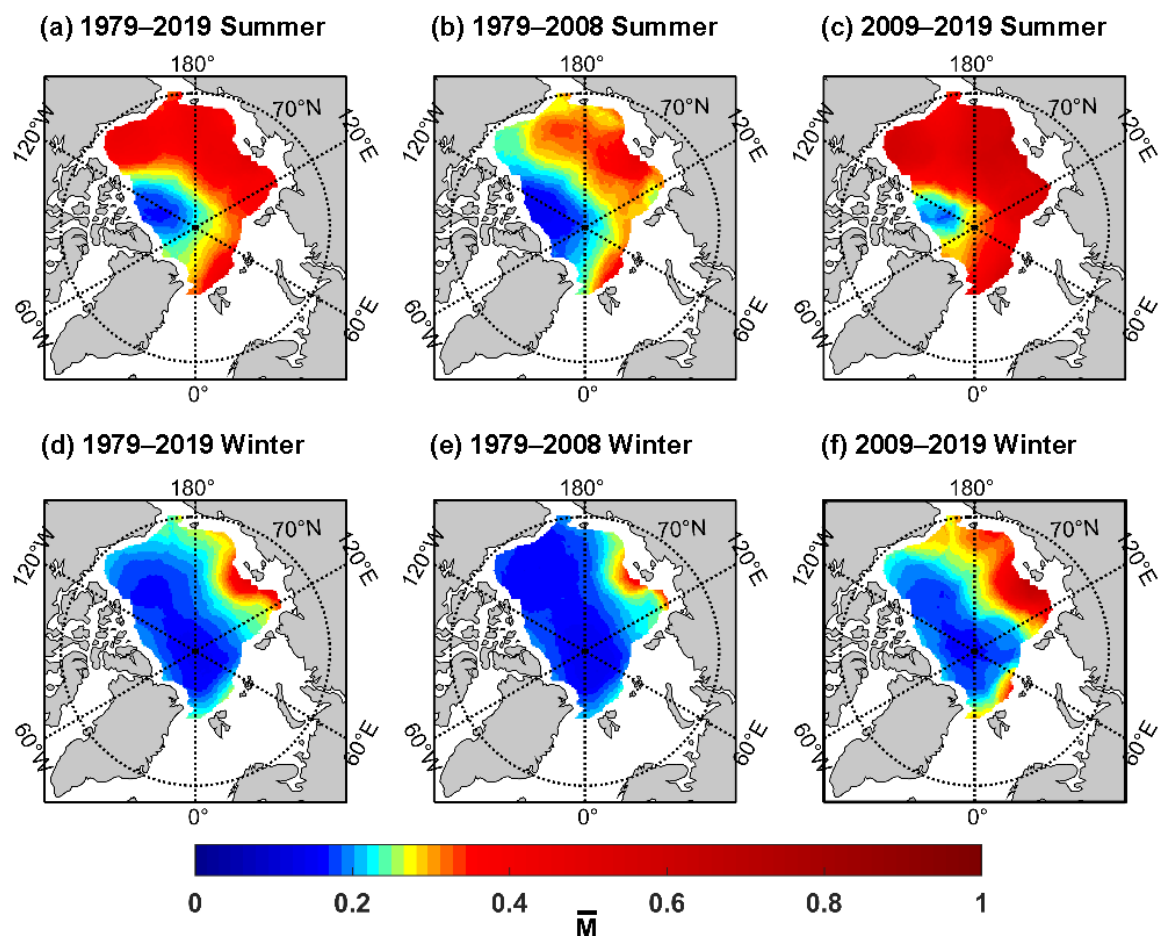


Figure 6. Spatial distributions of \bar{M} in summer (first row) and winter (second row) during (a,d) 1979–2019, (b,e) 1979–2008, (c,f) 2009–2019. The \bar{M} value for each grid is plotted only when the associated weight is greater than 1000.

As mentioned in Section 3.2, the SIIO are found to be strengthening significantly in summer during recent years. Figure 7a displays the spatial distribution of the \bar{M} difference in summer between the 2009–2019 period and the 1979–2008 period. There are obvious SIIO enhancements in the Beaufort Sea, East Siberian Sea and Laptev Sea. In order to investigate the possible reasons, the interannual trend in Arctic SIC in summer during 2009–2019 is calculated (Figure 7b). Similar to the pattern in Figure 7a, in the Beaufort Sea and East Siberian Sea where SIIO significantly increase, SIC also exhibits a distinct decline. Thus, it can be inferred that the enhancement of inertial oscillations in marginal seas in recent years is mainly related to the decrease in SIC. However, this does not rule out the influence of the decline of sea ice thickness and atmospheric factors such as the Arctic cyclones. Arctic cyclone activity shows a substantial increasing trend [42] and more storms have been observed in recent decades [43,44], which may have an impact on sea ice motion and enhance atmosphere–ice–ocean interactions. Based on in situ observations, Peng et al. [45] found the sea ice loss during the cyclone process accelerated. The accelerated melting of Arctic sea ice can be more vulnerable to storms, which, in turn, causes sea ice loss.

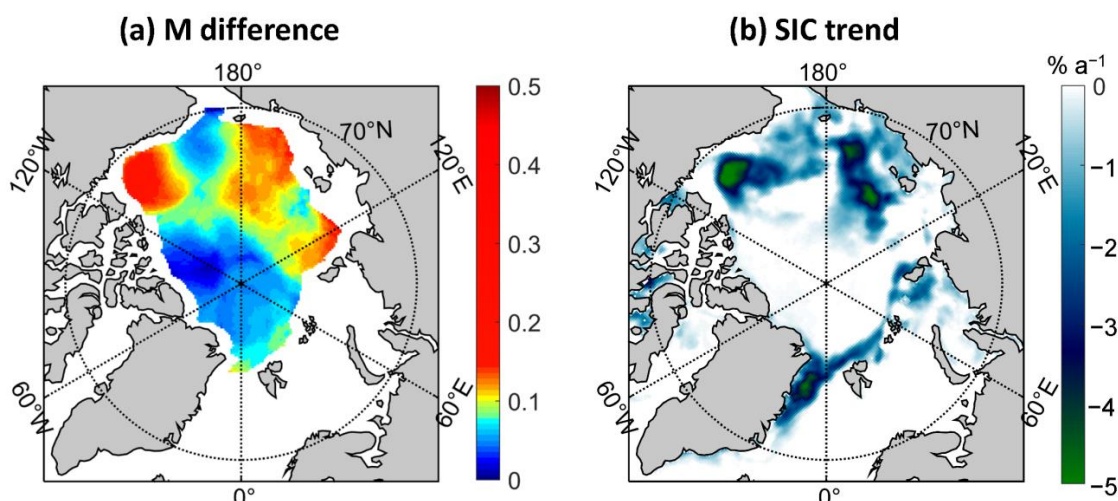


Figure 7. (a) Spatial distribution of the \bar{M} difference in summer between 2009–2019 and 1979–2008. (b) Spatial distribution of the interannual trend of sea ice concentration (SIC) during 2009–2019.

4. Discussion

The analysis from the IABP buoy dataset shows an enhancement of SIIO in the Arctic Ocean between 1979 and 2019. It should be noted that there is a heterogeneity in the spatial sampling of the IABP buoy dataset. A question arises as to whether the SIIO growth trend obtained in this study can reveal a realistic evolution of SIIO rather than the artificial aliases of the uneven spatial sampling of buoys. Gimbert et al. [29] have discussed this issue and indicated that the increase in M values during 1979–2008 cannot only be caused by the irregular sampling. In addition, the number of buoy data files has dramatically increased after 2008. It is necessary to explore this issue again owing to the extension of the time span of the IABP dataset. The new summer and winter datasets of M during 1979–2019 are constructed under the null hypothesis [29], which supposes a dataset satisfying the following condition: there is no temporal variation, but the spatial sampling of buoys at different locations in different periods will affect the overall trend estimated from this dataset. The construction step is as follows: for any buoy position at a given season, represented by the coordinate (X_j, Y_j) , all points in a circular region centered (X_j, Y_j) and with a radius of 200 km are considered to compute the M_0 values based on Equation (9). Figure 8 compares the multi-annual variations and trends of M_0 values under the null hypothesis and M values shown in Figure 4. The trend of M_0 values for 1979–2019 is $1.14 \times 10^{-3} (\pm 1.61 \times 10^{-3}) \text{ a}^{-1}$ in summer and $-0.004 \times 10^{-3} (\pm 0.33 \times 10^{-3}) \text{ a}^{-1}$ in winter, accounting for 14.5% and -0.2% of the trend of M values in summer and winter,

respectively. Consequently, the spatial heterogeneity of buoy sampling is not the reason for the increase in M values derived from the IABP buoy dataset. The increase in M values does indicate that the SIIO have been strengthening in the Arctic Ocean from 1979 to 2019.

Another problem is the contamination of tidal signals. In the whole Arctic Ocean, the semi-diurnal tidal period is close to the inertial period. Compared with other oceans, Arctic tides are weaker. The barotropic tidal model shows that there is weak tidal activity in the central Arctic Ocean but strong tidal amplitude over the Arctic continental shelves [46,47]. In this study, the data in the areas shorter than 150 km away from the coasts is excluded to avoid some aliases due to tides. However, high-value zones of \bar{M} near New Siberian Islands are found in both seasons, more remarkably in the winters of 1979–2008 (Figure 6), which may be a joint result of inertial and semi-diurnal tidal oscillations. As mentioned in Section 2.2, the normalized amplitude of the rotary spectrum at the inertial frequency is used to represent the SIIO strength, although it contains the semi-diurnal tidal component. Relatively strong tides near New Siberian Islands probably make us overestimate the magnitude of SIIO in these regions. Two cases of buoy trajectories (ID: 3004, 26 June 1999 to 25 July 1999; ID: 53095, 23 November 2019 to 22 December 2019) are displayed in Figure 9. For both cases, strong SIIO can be identified from the buoy tracks and the spectrum peaks at the inertial frequency $f \approx -2$ cycles d^{-1} . The semi-diurnal oscillation is evidenced by the peak at $f \approx 2$ cycles d^{-1} , whose amplitude is, respectively, 4.41 km d^{-1} for buoy (ID: 3004) and 8.83 km d^{-1} for buoy (ID: 53095). It can be seen from Figure 9b,d that although there is an obvious tidal peak, its contribution is far less than that of the near inertial motion, which ensures that the method used in this paper is feasible and reliable.

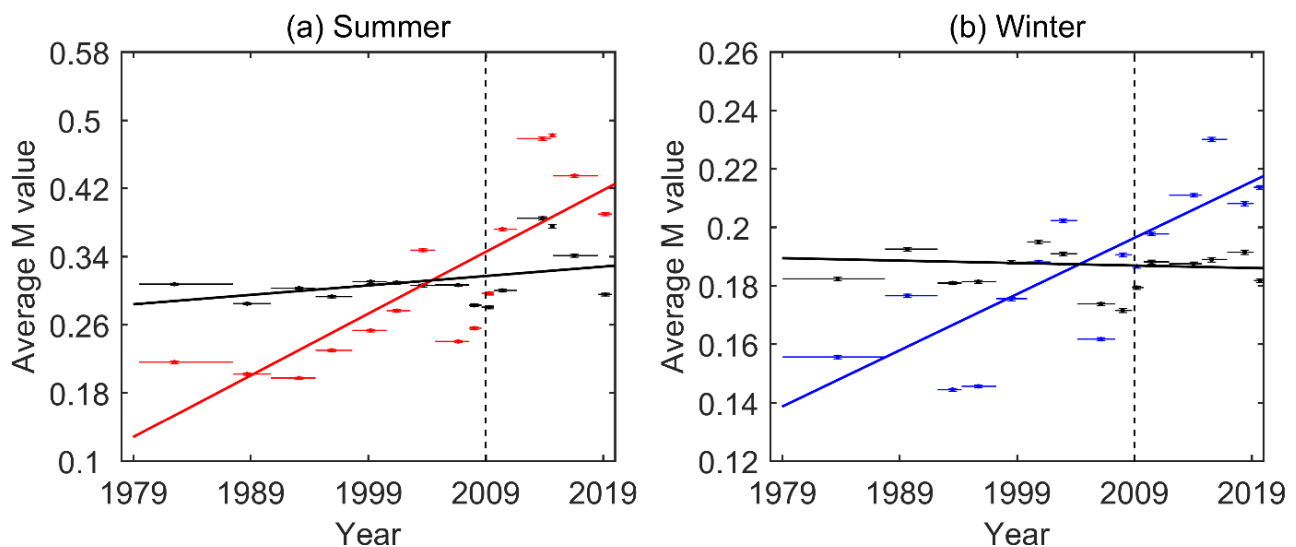


Figure 8. Multi-annual variation of M values in (a) summer and (b) winter during 1979–2019. The red lines in (a) and blue lines in (b) are same as those shown in Figure 4. The black lines in both panels are the multi-annual variations of M_0 values based on the null hypothesis. The fitting results in the least square sense can illustrate the effect of buoy spatial sampling on the trends derived from the IABP dataset.

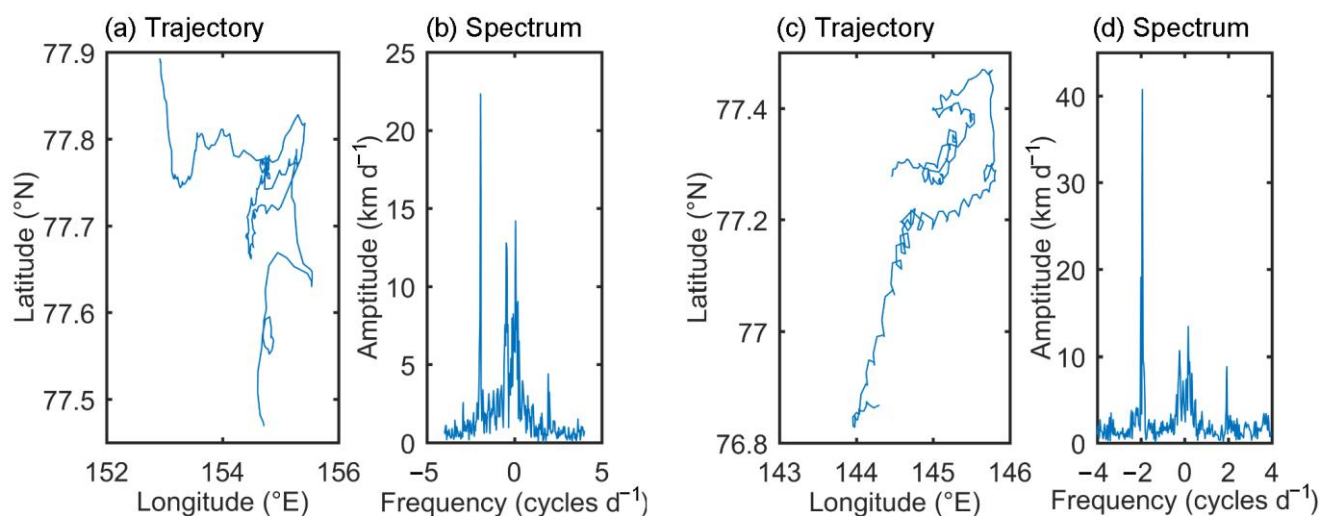


Figure 9. (a) The trajectory of IABP buoy (ID: 3004) from 26 June 1999 to 25 July 1999. (b) Rotary spectrum of the buoy drift velocity derived from the trajectory in (a). (c,d) Similar with (a,b), but for the IABP buoy (ID: 53095, 23 November 2019 to 22 December 2019).

In the Arctic Ocean, the presence of sea ice can substantially modulate energy input from the wind to the ocean [48,49]. The insulating effect of sea ice can damp the strength of internal waves generated by winds. With decreasing sea ice in recent decades, several works have discovered the increasing trend of near-inertial energy in the upper Arctic Ocean [50,51]. Furthermore, the complexity of sea ice morphology, especially the existence of ice ridges, directly strengthens the dynamic coupling process between the upper ocean and sea ice [52], thus significantly affecting the upper layer mixing. In global oceans, near-inertial waves and internal tides greatly contribute to diapycnal mixing [53–55], resulting in the redistribution of oceanic heat and momentum. Although the change of mixing effects has a direct impact on the Arctic circulation and water mass distribution [56], the effect of rapid sea ice decline on internal wave processes and its mixing effects are still poorly understood. This inspires us to focus on the process under the ice next and understand the interaction between atmosphere, the ice and the ocean based on the existing knowledge of SIIO.

5. Conclusions

Analyses derived from the IABP buoy dataset show a significant enhancement of SIIO in the Arctic Ocean between 1979 and 2019, with a more prominent increase in 2009–2019. From 1979 to 2019, the SIIO have been strengthening at a rate of 7.84×10^{-3} ($\pm 3.34 \times 10^{-3}$) a^{-1} in summer and 1.92×10^{-3} ($\pm 0.80 \times 10^{-3}$) a^{-1} in winter. Compared with 1979–2008, the SIIO magnitude increases by 66% in summer and 21% in winter. The SIIO enhancement in both seasons is found in most of the Arctic Ocean during 2009–2019, with more notable increases in the Beaufort Sea, East Siberian Sea and Laptev Sea in summer. The long-term strengthening of the SIIO between 1979 and 2019 is mainly associated with the decrease in sea ice thickness. The SIIO enhancement in the marginal seas in summer during 2009–2019 is expected to be highly correlated with the reduction of sea ice concentration, but this does not rule out the effect of the declining of sea ice thickness and atmospheric factors.

Author Contributions: Conceptualization, Q.L. and Z.X.; methodology, Q.L. and D.Y.; software, D.Y.; validation, D.Y.; formal analysis, D.Y.; investigation, D.Y.; resources, D.Y.; data curation, D.Y.; writing—original draft preparation, D.Y.; writing—review and editing, D.Y., Z.H., J.Y., Q.L., Z.X., P.Z. and B.Y.; visualization, D.Y.; supervision, Z.X., Q.L. and B.Y.; project administration, Z.X., Q.L. and B.Y.; funding acquisition, Z.X., Q.L. and B.Y. All authors have read and agreed to the published version of the manuscript.

Funding: This study was funded by the National Key Research and Development Plan of China (2019YFE0105700), the Scientific and Technological Innovation Project financially supported by Laoshan Laboratory (LSKJ202202502), the National Natural Science Foundation of China (92058202, 42176244), the Strategic Priority Research Program of Chinese Academy of Sciences (XDB42000000, XDA22050202) and the CAS Key Deployment Project of Centre for Ocean Mega-Research of Science (COMS2020Q07).

Institutional Review Board Statement: Not applicable.

Informed Consent Statement: Not applicable.

Data Availability Statement: The datasets for this study are publicly available. The buoy dataset is provided by the International Arctic Buoy Program (IABP) via <https://iabp.apl.uw.edu/data.html> (accessed on 27 December 2022). The passive-microwave-derived sea ice concentration (SIC) provided by the National Snow and Ice Data Center (NSIDC) can be downloaded via <https://nsidc.org/data/g02202/versions/4> (accessed on 27 December 2022).

Conflicts of Interest: The authors declare no conflict of interest. The funders had no role in the design of the study; in the collection, analyses, or interpretation of data; in the writing of the manuscript; or in the decision to publish the results.

References

1. Cavalieri, D.J.; Parkinson, C.L. Arctic sea ice variability and trends, 1979–2010. *Cryosphere* **2012**, *6*, 881–889. [\[CrossRef\]](#)
2. Onarheim, I.H.; Eldevik, T.; Smedsrud, L.H.; Stroeve, J.C. Seasonal and Regional Manifestation of Arctic Sea Ice Loss. *J. Clim.* **2018**, *31*, 4917–4932. [\[CrossRef\]](#)
3. Stroeve, J.; Notz, D. Changing state of Arctic sea ice across all seasons. *Environ. Res. Lett.* **2018**, *13*, 103001. [\[CrossRef\]](#)
4. Kwok, R.; Cunningham, G.F. Variability of Arctic sea ice thickness and volume from CryoSat-2. *Philos. Trans. A Math Phys. Eng. Sci.* **2015**, *373*, 20140157. [\[CrossRef\]](#)
5. Kwok, R. Arctic sea ice thickness, volume, and multiyear ice coverage: Losses and coupled variability (1958–2018). *Environ. Res. Lett.* **2018**, *13*, 105005. [\[CrossRef\]](#)
6. Tschudi, M.; Stroeve, J.; Stewart, J. Relating the Age of Arctic Sea Ice to its Thickness, as Measured during NASA’s ICESat and IceBridge Campaigns. *Remote Sens.* **2016**, *8*, 457. [\[CrossRef\]](#)
7. Rampal, P.; Weiss, J.; Marsan, D. Positive trend in the mean speed and deformation rate of Arctic sea ice, 1979–2007. *J. Geophys. Res.* **2009**, *114*, C05013. [\[CrossRef\]](#)
8. Wang, K.; Wang, C. Modeling linear kinematic features in pack ice. *J. Geophys. Res.* **2009**, *114*, C12011. [\[CrossRef\]](#)
9. Tremblay, L.-B.; Mysak, L.A. Modeling Sea Ice as a Granular Material, Including the Dilatancy Effect. *J. Phys. Oceanogr.* **1997**, *27*, 2342–2360. [\[CrossRef\]](#)
10. Martin, T.; Gerdes, R. Sea ice drift variability in Arctic Ocean Model Intercomparison Project models and observations. *J. Geophys. Res.* **2007**, *112*, C04S10. [\[CrossRef\]](#)
11. Heil, P.; Massom, R.A.; Allison, I.; Worby, A.P.; Lytle, V.I. Role of off-shelf to on-shelf transitions for East Antarctic sea ice dynamics during spring 2003. *J. Geophys. Res.* **2009**, *114*, C09010. [\[CrossRef\]](#)
12. Kwok, R. Observational assessment of Arctic Ocean sea ice motion, export, and thickness in CMIP3 climate simulations. *J. Geophys. Res.* **2011**, *116*, C00D05. [\[CrossRef\]](#)
13. Tschudi, M.A.; Meier, W.N.; Stewart, J.S. An enhancement to sea ice motion and age products at the National Snow and Ice Data Center (NSIDC). *Cryosphere* **2020**, *14*, 1519–1536. [\[CrossRef\]](#)
14. Zhang, J.; Rothrock, D.A. Modeling Global Sea Ice with a Thickness and Enthalpy Distribution Model in Generalized Curvilinear Coordinates. *Mon. Weather. Rev.* **2003**, *131*, 845–861. [\[CrossRef\]](#)
15. Fu, D.; Liu, B.; Qi, Y.; Yu, G.; Huang, H.; Qu, L. Multiscale variations in Arctic sea ice motion and links to atmospheric and oceanic conditions. *Cryosphere* **2021**, *15*, 3797–3811. [\[CrossRef\]](#)
16. Cox, K.A.; Stanford, J.D.; McVicar, A.J.; Rohling, E.J.; Heywood, K.J.; Bacon, S.; Bolshaw, M.; Dodd, P.A.; De la Rosa, S.; Wilkinson, D. Interannual variability of Arctic sea ice export into the East Greenland Current. *J. Geophys. Res. Ocean.* **2010**, *115*, C12063. [\[CrossRef\]](#)
17. Moritz, R.; Woodgate, R.; Zhang, J. Sea Ice Response to Atmospheric and Oceanic Forcing in the Bering Sea. *J. Phys. Oceanogr.* **2010**, *40*, 1729–1747. [\[CrossRef\]](#)
18. Howell, S.E.L.; Komarov, A.S.; Dabhoor, M.; Montpetit, B.; Brady, M.; Scharien, R.K.; Mahmud, M.S.; Nandan, V.; Geldsetzer, T.; Yackel, J.J. Comparing L- and C-band synthetic aperture radar estimates of sea ice motion over different ice regimes. *Remote Sens. Environ.* **2018**, *204*, 380–391. [\[CrossRef\]](#)
19. Kwok, R.; Schweiger, A.; Rothrock, D.A.; Pang, S.; Kottmeier, C. Sea ice motion from satellite passive microwave imagery assessed with ERS SAR and buoy motions. *J. Geophys. Res. Ocean.* **1998**, *103*, 8191–8214. [\[CrossRef\]](#)
20. Laverne, T.; Eastwood, S.; Teffah, Z.; Schyberg, H.; Breivik, L.A. Sea ice motion from low-resolution satellite sensors: An alternative method and its validation in the Arctic. *J. Geophys. Res. Ocean.* **2010**, *115*, C10032. [\[CrossRef\]](#)
21. Meier, W.N.; Dai, M. High-resolution Sea-ICE motions from AMSR-E imagery. *Ann. Glaciol.* **2010**, *44*, 352–356. [\[CrossRef\]](#)

22. Tschudi, M.; Fowler, C.; Maslanik, J.; Stroeve, J. Tracking the Movement and Changing Surface Characteristics of Arctic Sea Ice. *IEEE J. Sel. Top. Appl. Earth Obs. Remote Sens.* **2010**, *3*, 536–540. [\[CrossRef\]](#)
23. Brunette, C.; Tremblay, L.B.; Newton, R. A new state-dependent parameterization for the free drift of sea ice. *Cryosphere* **2022**, *16*, 533–557. [\[CrossRef\]](#)
24. Olason, E.; Notz, D. Drivers of variability in Arctic sea-ice drift speed. *J. Geophys. Res. Ocean.* **2014**, *119*, 5755–5775. [\[CrossRef\]](#)
25. Zhang, F.; Pang, X.; Lei, R.; Zhai, M.; Zhao, X.; Cai, Q. Arctic sea ice motion change and response to atmospheric forcing between 1979 and 2019. *Int. J. Climatol.* **2021**, *42*, 1854–1876. [\[CrossRef\]](#)
26. Lei, R.; Heil, P.; Wang, J.; Zhang, Z.; Li, Q.; Li, N. Characterization of sea-ice kinematic in the Arctic outflow region using buoy data. *Polar Res.* **2016**, *35*, 22658. [\[CrossRef\]](#)
27. Heil, P.; Hutchings, J.K.; Worby, A.P.; Johansson, M.; Launiainen, J.; Haas, C.; Hibler, W.D. Tidal forcing on sea-ice drift and deformation in the western Weddell Sea in early austral summer, 2004. *Deep. Sea Res. Part II Top. Stud. Oceanogr.* **2008**, *55*, 943–962. [\[CrossRef\]](#)
28. Hibler, W.D.; Weeks, W.F.; Kovacs, A.; Ackley, S.F. Differential Sea-Ice Drift. I. Spatial and Temporal Variations in Sea-Ice Deformation. *J. Glaciol.* **1974**, *13*, 437–455. [\[CrossRef\]](#)
29. Gimbert, F.; Marsan, D.; Weiss, J.; Jourdain, N.C.; Barnier, B. Sea ice inertial oscillations in the Arctic Basin. *Cryosphere* **2012**, *6*, 1187–1201. [\[CrossRef\]](#)
30. Lei, R.; Gui, D.; Hutchings, J.K.; Heil, P.; Li, N. Annual Cycles of Sea Ice Motion and Deformation Derived From Buoy Measurements in the Western Arctic Ocean Over Two Ice Seasons. *J. Geophys. Res. Ocean.* **2020**, *125*, e2019JC015310. [\[CrossRef\]](#)
31. Heil, P.; Hibler, W.D. Modeling the High-Frequency Component of Arctic Sea Ice Drift and Deformation. *J. Phys. Oceanogr.* **2002**, *32*, 3039–3057. [\[CrossRef\]](#)
32. Hunkins, K. Inertial oscillations of Fletcher’s Ice Island (T-3). *J. Geophys. Res.* **1967**, *72*, 1165–1174. [\[CrossRef\]](#)
33. Kawaguchi, Y.; Koenig, Z.; Nomura, D.; Hoppmann, M.; Inoue, J.; Fang, Y.C.; Schulz, K.; Gallagher, M.; Katlein, C.; Nicolaus, M.; et al. Turbulent Mixing During Late Summer in the Ice–Ocean Boundary Layer in the Central Arctic Ocean: Results From the MOSAiC Expedition. *J. Geophys. Res. Ocean.* **2022**, *127*, e2021JC017975. [\[CrossRef\]](#)
34. Urbancic, G.H.; Lamb, K.G.; Fer, I.; Padman, L. The Generation of Linear and Nonlinear Internal Waves Forced by Subinertial Tides over the Yermak Plateau, Arctic Ocean. *J. Phys. Oceanogr.* **2022**, *52*, 2183–2203. [\[CrossRef\]](#)
35. Kawaguchi, Y.; Itoh, M.; Fukamachi, Y.; Moriya, E.; Onodera, J.; Kikuchi, T.; Harada, N. Year-round observations of sea-ice drift and near-inertial internal waves in the Northwind Abyssal Plain, Arctic Ocean. *Polar Sci.* **2019**, *21*, 212–223. [\[CrossRef\]](#)
36. Beasley, W.H.; Rodgers, J.L. Bootstrapping and Monte Carlo methods. In *Book APA handbook of research methods in psychology*, 22nd ed.; Cooper, H., Camic, P.M., Long, D.L., Panter, A.T., Rindskopf, D., Sher, K.J., Eds.; American Psychological Association: Washington, WA, USA, 2012; Volume 2, pp. 407–425.
37. Spreen, G.; Kwok, R.; Menemenlis, D. Trends in Arctic sea ice drift and role of wind forcing: 1992–2009. *Geophys. Res. Lett.* **2011**, *38*, L19501. [\[CrossRef\]](#)
38. Thorndike, A.S.; Colony, R. Sea ice motion in response to geostrophic winds. *J. Geophys. Res.* **1982**, *87*, 5845–5852. [\[CrossRef\]](#)
39. Reifenberg, S.F.; Goessling, H.F. Predictability of Arctic sea ice drift in coupled climate models. *Cryosphere* **2022**, *16*, 2927–2946. [\[CrossRef\]](#)
40. Gimbert, F.; Jourdain, N.C.; Marsan, D.; Weiss, J.; Barnier, B. Recent mechanical weakening of the Arctic sea ice cover as revealed from larger inertial oscillations. *J. Geophys. Res. Ocean.* **2012**, *117*, C00J12. [\[CrossRef\]](#)
41. Howell, S.E.L.; Wohleben, T.; Daboor, M.; Derksen, C.; Komarov, A.; Pizzolato, L. Recent changes in the exchange of sea ice between the Arctic Ocean and the Canadian Arctic Archipelago. *J. Geophys. Res. Ocean.* **2013**, *118*, 3595–3607. [\[CrossRef\]](#)
42. Barrett, A.P.; Serreze, M.C. The Summer Cyclone Maximum over the Central Arctic Ocean. *J. Clim.* **2008**, *21*, 1048–1065. [\[CrossRef\]](#)
43. Aizawa, T.; Tanaka, H.L. Axisymmetric structure of the long lasting summer Arctic cyclones. *Polar Sci.* **2016**, *10*, 192–198. [\[CrossRef\]](#)
44. Tao, W.; Zhang, J.; Zhang, X. The role of stratosphere vortex downward intrusion in a long-lasting late-summer Arctic storm. *Q. J. R. Meteorol. Soc.* **2017**, *143*, 1953–1966. [\[CrossRef\]](#)
45. Peng, L.; Zhang, X.; Kim, J.H.; Cho, K.H.; Kim, B.M.; Wang, Z.; Tang, H. Role of Intense Arctic Storm in Accelerating Summer Sea Ice Melt: An In Situ Observational Study. *Geophys. Res. Lett.* **2021**, *48*, e2021GL092714. [\[CrossRef\]](#)
46. Padman, L.; Erofeeva, S. A barotropic inverse tidal model for the Arctic Ocean. *Geophys. Res. Lett.* **2004**, *31*, L02303. [\[CrossRef\]](#)
47. Baumann, T.M.; Polyakov, I.V.; Padman, L.; Danielson, S.; Fer, I.; Janout, M.; Williams, W.; Pnyushkov, A.V. Arctic tidal current atlas. *Sci. Data* **2020**, *7*, 275. [\[CrossRef\]](#)
48. Martini, K.I.; Simmons, H.L.; Stoudt, C.A.; Hutchings, J.K. Near-Inertial Internal Waves and Sea Ice in the Beaufort Sea*. *J. Phys. Oceanogr.* **2014**, *44*, 2212–2234. [\[CrossRef\]](#)
49. You, J.; Xu, Z.; Robertson, R.; Li, Q.; Yin, B. Geographical inhomogeneity and temporal variability of mixing property and driving mechanism in the Arctic Ocean. *J. Oceanol. Limnol.* **2022**, *40*, 846–869. [\[CrossRef\]](#)
50. Dosser, H.V.; Rainville, L. Dynamics of the Changing Near-Inertial Internal Wave Field in the Arctic Ocean. *J. Phys. Oceanogr.* **2016**, *46*, 395–415. [\[CrossRef\]](#)
51. Polyakov, I.V.; Rippeth, T.P.; Fer, I.; Baumann, T.M.; Carmack, E.C.; Ivanov, V.V.; Janout, M.; Padman, L.; Pnyushkov, A.V.; Rember, R. Intensification of Near-Surface Currents and Shear in the Eastern Arctic Ocean. *Geophys. Res. Lett.* **2020**, *47*, e2020GL089469. [\[CrossRef\]](#)

52. Zhang, P.; Xu, Z.; Li, Q.; You, J.; Yin, B.; Robertson, R.; Zheng, Q. Numerical Simulations of Internal Solitary Wave Evolution Beneath an Ice Keel. *J. Geophys. Res. Ocean.* **2022**, *127*, e2020JC017068. [[CrossRef](#)]
53. Xu, Z.; Yin, B.; Hou, Y.; Xu, Y. Variability of internal tides and near-inertial waves on the continental slope of the northwestern South China Sea. *J. Geophys. Res. Ocean.* **2013**, *118*, 197–211. [[CrossRef](#)]
54. Xu, Z.; Wang, Y.; Liu, Z.; McWilliams, J.C.; Gan, J. Insight Into the Dynamics of the Radiating Internal Tide Associated With the Kuroshio Current. *J. Geophys. Res. Ocean.* **2021**, *126*, e2020JC017018. [[CrossRef](#)]
55. Nam, S.; Chen, X. Oceanic Internal Waves and Internal Tides in the East Asian Marginal Seas. *J. Mar. Sci. Eng.* **2022**, *10*, 573. [[CrossRef](#)]
56. Liang, X.; Losch, M. On the Effects of Increased Vertical Mixing on the Arctic Ocean and Sea Ice. *J. Geophys. Res. Ocean.* **2018**, *123*, 9266–9282. [[CrossRef](#)]

Disclaimer/Publisher’s Note: The statements, opinions and data contained in all publications are solely those of the individual author(s) and contributor(s) and not of MDPI and/or the editor(s). MDPI and/or the editor(s) disclaim responsibility for any injury to people or property resulting from any ideas, methods, instructions or products referred to in the content.